Commun. Comput. Phys.
doi: 10.4208/cicp.OA-2016-0165

Vol. **22**, No. 3, pp. 712-741
September 2017

Comprehensive Studies on Rarefied Jet and Jet Impingement Flows with Gaskinetic Methods

Chunpei Cai*, Xin He and Kai Zhang

Department of Mechanical Engineering and Engineering Mechanics, Michigan Technological University, Houghton, Michigan, 49931, USA.

Communicated by Kun Xu

Received 29 September 2016; Accepted (in revised version) 16 December 2016

Abstract. This paper presents comprehensive studies on two closely related problems of high speed collisionless gaseous jet from a circular exit and impinging on an inclined rectangular flat plate, where the plate surface can be diffuse or specular reflective. Gaskinetic theories are adopted to study the problems, and several crucial geometry-location and velocity-direction relations are used. The final complete results include flowfield properties such as density, velocity components, temperature and pressure, and impingement surface properties such as coefficients of pressure, shear stress and heat flux. Also included are the averaged coefficients for pressure, friction, heat flux, moment over the whole plate, and the averaged distance from the moment center to the plate center. The final results include complex but accurate integrations involving the geometry and specific speed ratios, inclination angle, and the temperature ratio. Several numerical simulations with the direct simulation Monte Carlo method validate these analytical results, and the results are essentially identical. Exponential, trigonometric, and error functions are embedded in the solutions. The results illustrate that the past simple cosine function approach is rather crude, and should be used cautiously. The gaskinetic method and processes are heuristic and can be used to investigate other external high Knudsen number impingement flow problems, including the flowfield and surface properties for high Knudsen number jet from an exit and flat plate of arbitrary shapes. The results are expected to find many engineering applications.

AMS subject classifications: 82C40, 76P05, 65C05

Key words: Kinetic theory of gases, rarefied gas flows, Monte Carlo methods.

1 Introduction

Gaseous jets expanding into a vacuum and jet impingement on a plate are two fundamental fluid dynamic problems with many reports in the literature. As the counterpart

*Corresponding author. *Email addresses:* ccai@mtu.edu (C. Cai), xinhe@mtu (X. He), kazhang@mtu.edu (K. Zhang)

 ©2017 Global-Science Press

https://doi.org/10.4208/cicp.OA-2016-0165 Published online by Cambridge University Press

to the continuum flow situation, highly rarefied jet and jet impingement flows provide bounding limits and insights to many problems by solely including molecular movements. In many applications involving high Knudsen (Kn) numbers or high speed velocities, the contributions from particle collisions are insignificant. One important example is atomic/molecular beams [1,2] which lead to many important discoveries. Other nontrivial applications include materials processing inside vacuum chambers [3] and rocket plume effects [4,5].

Because there are so many applications related with the rarefied jet and jet impingement, it is challenging to provide a detailed review. Here we only provide several examples for rocket plume, which is crucial to the rocket and spacecraft community. As the most important signature, rocket plume is a key component for space propulsion, inferred radar detections and performance evaluations. Due to this importance, many communities have been investigating rarefied gaseous jet/plume impingement flows for decades. For example, the biennial international rarefied gasdynamics symposiums usually collect papers on gaseous jet/jet impingement and molecular beams; the NASA Johnson Space Center developed a versatile particle simulation package to simulate plume impingement [6] on spacecraft surface. Kannenberg and Boyd [7]used the cosine law and the Simons model [8] and particle simulation method to compute the density of a plume impinging on a flat plate. Ivanov [9] and his colleagues performed particle simulations of plume flows from a nozzle.

Compressible flows usually can be divided into four categories according to the Knudsen number (Kn) [10]:

$$Kn = \lambda / L, \tag{1.1}$$

where λ is the molecular mean free path, and L is a characteristic length. These four regimes are: continuum ($0 < Kn < 0.01$), velocity slip and temperature jump ($0.01 < Kn < 0.1$), transitional ($0.1 < Kn < 10$), and free molecular or collisionless ($Kn > 10$). For jet and jet impingement on a flat plate, there are abundant studies concentrating in the continuum regime, and many numerical studies at the transition regime; at the collisionless flow regime, there are numerical and experimental studies on the flowfield and surface properties. For high speed, gaseous, collisionless flows out of an exit, many past studies adopted several simplifications. For example, Noller [11] proposed a solid angle treatment to implicitly consider the nozzle exit geometry and obtained the plume density field expressed with integrations over solid angles which are subtended by a flowfield point and many small surface elements; the cosine law/Simons model [8] treats a rocket plume as from a point source; Narasimha's early investigation [12] indicated that the plume solution is rather complicated with many cosine functions. Another rocket plume treatment, which is also based on collisionless flows, was suggested by Woronowicz [13]. His treatment splits the exit into many small segments, as such, the density and pressure distributions in the flowfield can be computed numerically. Further, he proposed the concept of starting surfaces alleviating the difficulty of this problem.

This paper presents recent work on seeking exact solutions to the problems of colli-

https://doi.org/10.4208/cicp.OA-2016-0165 Published online by Cambridge University Press

sionless circular jet expanding into a vacuum and jet impingement on an inclined rectangular plate with a diffuse or specular surface. A diffuse reflection means when a particle collides at a surface, it recoils uniformly inside the solid angle in a local plane. For a circular plate surface, the solid angle forms a span of 2π. For a specular reflection case, the reflected particles' normal velocities are reversed, while the tangent moment maintains unchanged. Recently, detailed solutions for collisionless two-dimensional and circular plume flows were developed and reported [14–19] followed with progress on the corresponding plume impingement problems [20]. These plume solutions only consider collisionless flow situations, such as those plasma flows firing from an electric propulsion device. The collision effects are completely neglected; and for the impingement problem, only surface properties and diffuse reflections are considered. Different from other work in the past, this paper concentrates on analytical studies of highly rarefied jet and jet impingement flows, and provides many detailed, complex, but exact and ultimate solutions for the flowfield and surface properties. Because the final expressions are quite complex, several particle simulations are performed for validations.

The paper is organized as follows: Section 2 presents past results on collisionless gaseous circular jet expanding into a vacuum, and these exact solutions serve as the foundations to investigate the impingement flow problem; Section 3 presents the plate surface properties; Sections 4 and 5 present exact flowfield solutions to the corresponding jet impingement on an inclined rectangular flat plate with a diffuse and a specular surface, respectively; Section 6 compares the exact analytical solutions and direct simulation Monte Carlo (DSMC) [21] validation results; and lastly Section 7 summarizes this paper with several conclusions.

2 Collisionless free plume expanding into a vacuum

For the problem of a rarefied plume/jet expanding into a vacuum, there are many published papers in the literature. For example, the work by Boyd [22] implemented the Simons model, the method of characteristics (MOC), and several DSMC simulations. The first two methods are derived with continuum conditions. Simulations of hydrazine thruster plume were performed [23] and the DSMC technique was determined to be the most suitable for treating collisional behaviors of the gas. The effects from the nozzle lip and backflow expansion regions were also studied. The DSMC method is quite different from the traditional computational fluid dynamics which are based on the continuum flow assumption. The DSMC method decouples the particle movements and collisions, and many physical models, for example [24], can be conveniently incorporated into the method.

The problem of high Kn number, high speed jet expanding into a vacuum can also be studied with the gaskinetic theory and analytical expressions obtained. This section presents those results, including number density, velocity components, and temperature at any point $P(X,Y,Z)$ in front of a circular nozzle. Even though a collisionless flow

https://doi.org/10.4208/cicp.OA-2016-0165 Published online by Cambridge University Press

assumption is adopted, these final expressions are applicable to higher density jet/plume because molecules barely have enough time to collide within concerned regions due to the high speed. This problem of a free jet expansion into a vacuum is the foundation for the jet impingement problem, and details can be found in another paper [19]. To be concise, we only list crucial points and the results in this section.

Figs. 1 and 2 illustrate the problem of collisionless plume impinging on an inclined diffuse plate and the corresponding thermal velocity phases for those particles at a specific point $P(X,Y,Z)$. If we neglect the plate effects and only consider the plume parts represented by the left parts of these two figures, then the plume impingement problem degenerates to a free plume expansion problem.

From the gaskinetic theories, it is assumed the thermal velocities of those molecules leaving the exit are characterized by the following Maxwellian velocity distribution function (VDF):

$$f_0(0,y,z)=n_0\left(\frac{\beta_0}{\pi}\right)^{3/2}\exp\left[-\beta_0(u^2+v^2+w^2)\right], \tag{2.1}$$

where n_0 is the number density, $\beta_0=1/(2RT_0)$, and R is the gas constant for specific species. Further, with a known VDF $f(u,v,w)$ at a point $P(X,Y,Z)$, the average number density normalized by a reference value and velocities at this point can be evaluated as [10]:

$$n(X,Y,Z)=\iiint_{\Omega} f(u,v,w)dudvdw, \tag{2.2}$$

$$U(X,Y,Z)=\frac{1}{n(X,Y,Z)}\iiint_{\Omega} uf(u,v,w)dudvdw, \tag{2.3}$$

$$V(X,Y,Z)=\frac{1}{n(X,Y,Z)}\iiint_{\Omega} vf(u,v,w)dudvdw, \tag{2.4}$$

$$W(X,Y,Z)=\frac{1}{n(X,Y,Z)}\iiint_{\Omega} wf(u,v,w)dudvdw, \tag{2.5}$$

$$T(X,Y,Z)=\frac{1}{3Rn(X,Y,Z)}\iiint_{\Omega} (C_1^2+C_2^2+C_3^2)fdudvdw, \tag{2.6}$$

where Ω is the integration domain in the velocity phase; u, v, and w are the instantaneous velocity components; C_1, C_2, and C_3 are the thermal velocity components. Hence, the critical steps to compute the flowfield properties are to obtain the VDFs and the integral domains.

The velocity components of those particles escaping from point $(0,y,z)$ at the circular nozzle and arriving at point $P(X,Y,Z)$ must satisfy the following constrain condition, which was revealed recently [19,20]:

$$\frac{X}{u+U_0}=\frac{Y-y}{v}=\frac{Z-z}{w}, \tag{2.7}$$

https://doi.org/10.4208/cicp.OA-2016-0165 Published online by Cambridge University Press

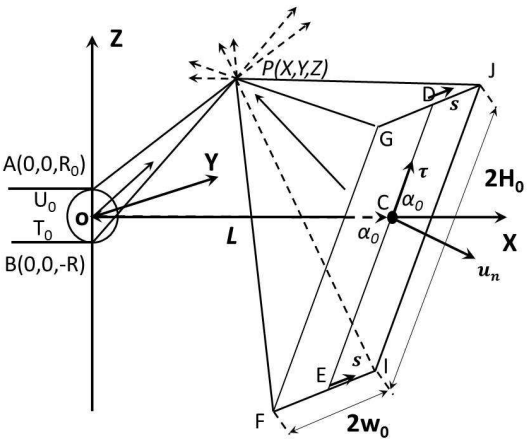


Figure 1: Illustration of the Diffuse Reflective Plate Impingement Problem.

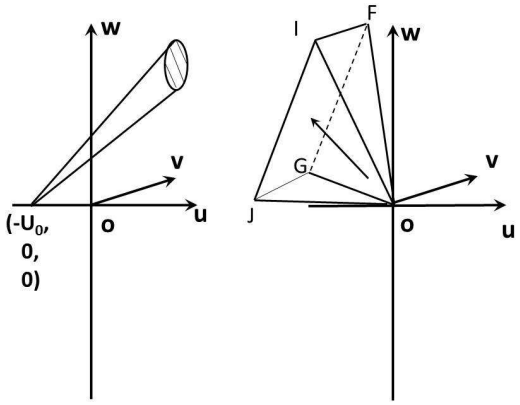


Figure 2: Thermal Velocity Phases for the Diffuse Reflective Plate Impingement Problem. Left: jet; right: reflected particles.

here, $y=r\cos\theta$, $z=r\sin\theta$ and r, θ are the local coordinates for the circular exit. If the bulk gas velocity is U_0 at the exit, the integration domain vertex shall shift to $(-U_0,0,0)$ to compensate the effects. This approach allows us to unify the expressions for VDFs, and the integrations to obtain bulk properties can be performed with multiple integration domains. This relation is quite fundamental. Those particles starting from the exit and arriving at a specific flowfield form a special velocity domain, and because there are no collisions involved, the velocity domain must is the same for the flowfield point $P(X,Y,Z)$. The next natural step is to integrate the macroscopic properties according to the gaskinetic formulas, Eqs. (2.2)-(2.6). Bearing in mind that the velocity phase for the point $P(X,Y,Z)$ has an oblique conic shape with an infinite length, it is desirable to utilize a change of variables to transform the integration domain to a finite domain. From the constrain condition, the velocity components of the particles in y and z direction can be written as:

$$v=\frac{Y-r\cos\theta}{X}(u+U_0); \qquad w=\frac{Z-r\sin\theta}{X}(u+U_0). \tag{2.8}$$

The above two equations provide us a change of variables by using the Jacobian transformation:

$$dvdw=\frac{(u+U_0)^2}{X^2}rdrd\theta,$$

the integration domain changes from a semi-infinite domain involving u,v,w to a finite domain related to nozzle exit geometry, r and θ.

Based on the classical gaskinetic theory in the literature, there are work and results for the flowfield density, velocity, and temperatures at point $P(X,0,Z)$ for the axisymmetric situation [19, 20]. In this work, more general solutions for point $P(X,Y,Z)$ are needed because the impingement problems to be investigated next are three-dimensional with

https://doi.org/10.4208/cicp.OA-2016-0165 Published online by Cambridge University Press

the results listed as follows:

$$\frac{n_j(X,Y,Z)}{n_0}=\frac{e^{-S_0^2}}{\sqrt{\pi^3}X^2}\int_0^{2\pi}d\theta\int_0^{R_0}\frac{A_0}{Q^3}rdr, \tag{2.9}$$

$$\frac{U_j(X,Y,Z)}{\sqrt{2RT_0}}=\frac{e^{-S_0^2}}{\sqrt{\pi^3}X^2}\frac{n_0}{n_j}\int_0^{2\pi}d\theta\int_0^{R_0}\frac{A_1}{Q^4}rdr, \tag{2.10}$$

$$\frac{V_j(X,Y,Z)}{\sqrt{2RT_0}}=\frac{e^{-S_0^2}}{\sqrt{\pi^3}X^3}\frac{n_0}{n_j}\int_0^{2\pi}d\theta\int_0^{R_0}(Y-r\cos\theta)\frac{A_1}{Q^4}rdr, \tag{2.11}$$

$$\frac{W_j(X,Y,Z)}{\sqrt{2RT_0}}=\frac{e^{-S_0^2}}{\sqrt{\pi^3}X^3}\frac{n_0}{n_j}\int_0^{2\pi}d\theta\int_0^{R_0}(Z-r\sin\theta)\frac{A_1}{Q^4}rdr, \tag{2.12}$$

$$\frac{T_j(X,Y,Z)}{T_0}=\frac{2}{3}\frac{e^{-S_0^2}}{\sqrt{\pi^3}X^2}\frac{n_0}{n_j}\int_0^{2\pi}d\theta\int_0^{R_0}\frac{A_2}{Q^3}rdr-\frac{U_j^2+V_j^2+W_j^2}{3RT_0}, \tag{2.13}$$

where

$$Q^2=\frac{X^2+Y^2+Z^2+r^2-2rY\cos\theta-2Zr\sin\theta}{X^2}, \tag{2.14}$$

$$A_0=\frac{\sqrt{\pi}}{4}[1+\mathrm{erf}(a)]e^{a^2}(1+2a^2)+\frac{a}{2}, \tag{2.15}$$

$$A_1=\frac{\sqrt{\pi}}{4}[1+\mathrm{erf}(a)]e^{a^2}(3a+2a^3)+\frac{1}{2}+\frac{a^2}{2}, \tag{2.16}$$

$$A_2=\frac{\sqrt{\pi}}{4}[1+\mathrm{erf}(a)]e^{a^2}\left(\frac{3}{2}+6a^2+2a^4\right)+\frac{5}{4}a+\frac{1}{2}a^3, \tag{2.17}$$

where $S_0=U_0/\sqrt{2RT_0}$ and $a=S_0/Q$. These formulas illustrate that the free plume flow-field solutions contain geometry factors of R, X, Y, Z, and the speed ratio S_0. As seen, the problem of a three-dimensional rarefied free plume expanding from a circular exit and into a vacuum has compact solution expressions.

At far field, traditionally the cosine law relation is used for the density results, i.e., at locations closer to the plume centerline, the density varies as cosine functions, but after a certain angle, the density drops as exponential functions. This can be explained conveniently from the above results. At farfield and close to the centerline, e.g., in plane $Z=0$, $X^2+Y^2\gg r^2-2rY\cos\theta$, $1/Q\approx\cos\gamma$, where γ is the angle formed by the plume direction and line PO. Correspondingly, Eq. (2.9) degenerates as:

$$\frac{n_j(X,Y,0)}{n_0}\approx\frac{R_0^2}{\sqrt{\pi}X^2}\left[\frac{\sqrt{\pi}}{4}[1+\mathrm{erf}(S_0\cos\gamma)]e^{-S_0^2\sin^2\gamma}(1+2S_0^2\cos^2\gamma)+\frac{S_0}{2}\cos\gamma e^{-S_0^2}\right]. \tag{2.18}$$

Evidently, there are factors of cosine functions and an exponential function involved in the above formula. With a larger angle γ, the term containing exponential term dominates, while for the smaller γ term scenario, the last term dominates. In the literature, Boyton [8] used complex boundary layer theory to discuss the transition behavior, in a continuum flow region. As shown above, for the high Kn number free jet flows, the

https://doi.org/10.4208/cicp.OA-2016-0165 Published online by Cambridge University Press

above expression offers a natural explanation. In the literature, different beam factors are adopted for better curve-fitting of different experimental results, however, the above complex expression may offer deeper insights. At farfield locations and far from the center, $\cos\gamma \approx 1$ and in plane $Z=0$, $Y \gg X$, Eq. (2.9) degenerates as:

$$\frac{n_j(X,Y,0)}{n_0} \approx \frac{e^{-S_0^2}}{2\sqrt{\pi}} \frac{R_0^2 X^2}{Y^4}. \tag{2.19}$$

As can be seen, there are no factors of cosine function; instead, at large but fixed ratio of X/Y, there is a dominate asymptote of $e^{-S_0^2}$ (i.e., an exponential function).

3 Diffuse and specular reflective plate surface properties

For the problem of plume flow impinging on a flat surface, the plate surface properties are more important than the flowfield properties because they are critical to compute pressure, friction, moment, and heat loads on the surface. As will be illustrated later, for the diffuse reflective plate scenario, plate surface properties, such as surface velocity slips on the plate surface, affect the flowfield properties. Due to these reasons, the surface properties are presented first.

During the past, much work assumed plume starts from a point surface. However, this treatment is not general enough to investigate the near field properties. The point source results cannot include the plate surface temperature factor, and usually merely offer approximations for the impingement flow density field, they do not include the velocity and pressure fields and surface properties.

This study abandons the point source assumption. An inclined flat plate is assumed to be set in front of a nozzle exit. The nozzle exit is assumed to have a radius of R_0, but the approach can be applied to any finite size nozzle exit with an arbitrary shape. The exit center is the coordinate origin. The plate inclination angle is α_0, and the center-center distance from the nozzle to the plate is L. We assume the plate has a rectangular shape; however, in general, it can apply to a plate of arbitrary shapes. The plate semi-width (horizontal direction) is W_0, the semi-height along the inclined direction is H_0. The gas at the nozzle exit plane is assumed to have a bulk number density of n_0, an average velocity U_0, and a temperature T_0. The plate temperature is assumed to be T_w.

Fig. 1 illustrates the situation for a free jet impinging on a diffuse reflective plate. The flowfield properties at point $P(X,Y,Z)$ have contributions from the free jet and the surface. For the plate surface properties, we assume the coordinates for a point on the plate are (X,Y,Z), which can also be represented by two local coordinates of (s,τ), along the plate surface: $-W_0 < s < W_0$, and $-H_0 < \tau < H_0$. Fig. 2 shows the velocity domain for the diffuse plate situation, the left side is for the free jet and it has an oblique cone shape starting from $(-U_0,0,0)$ and extends to infinity at the right. The right side velocity phase is for the contribution from the diffuse plate surface to the flowfield point $P(X,Y,Z)$. It has a pyramid shape with a vertex point $(0,0,0)$ and extends to infinity. Due to the

https://doi.org/10.4208/cicp.OA-2016-0165 Published online by Cambridge University Press

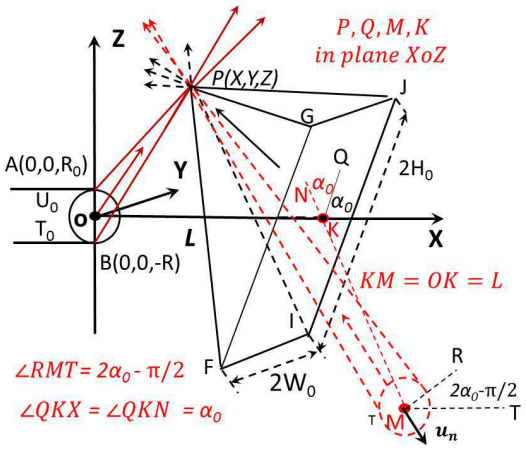


Figure 3: Illustration of the Specular Reflective Plate Impingement Problem.

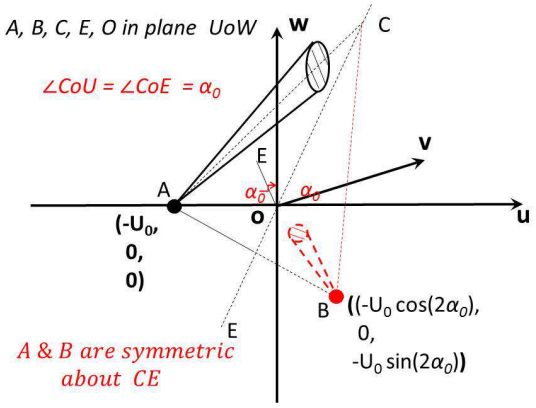


Figure 4: Thermal Velocity Phases for the Specular Reflective Plate Impingement Problem. Left: jet; right: virtual jet.

inclination angle, it is possible to have $-\infty<u<+\infty$, or $-\infty<v<+\infty$, or $-\infty<w<+\infty$. This situation is different from the normally set plate situation. There are parallel relations among these two figures; e.g., $PG\parallel OG$, $PJ\parallel OJ$, $FP\parallel OF$, and $PI\parallel OI$.

Figs. 3 and 4 show the corresponding specular reflective plate situation. The effect from the plate is equivalently treated by placing a virtual nozzle at the right side of the plate. The virtual nozzle is mirrored from the real nozzle. With this virtual nozzle, particles from the real nozzle can be considered absorbed when they collide at the specular plate surface. Those reflected particles are considered as new particles emitted from the virtual nozzle; hence, the specular plate effects can be considered when we compute the flowfield at the left side, and the plate is neglected. To satisfy the zero number flux or non-penetration condition at the specular plate surface, the virtual nozzle has a position of $(L-L\cos 2\alpha_0,0,-L\sin 2\alpha_0)$, and the velocity components are $(-U_0\cos 2\alpha_0,0,-U_0\sin 2\alpha_0)$, which has the same magnitude as the jet from the true nozzle. As such, two oblique cones are included in Fig. 3. The solid oblique cone represents the contribution from the true nozzle, while the dashed oblique cone for the virtual nozzle. Even though both oblique cones are bounded and extending to infinity, only the solid cone has a lower bound for the $u-$ component (i.e., $-U_0<u<+\infty$). This relation simplifies the later integrations. For the dashed cone, due to the inclination angle and the rotation relations, we cannot assert such a bounding relation for any velocity components. There are also parallel relations among these two figures: for example, $PO\parallel AC$, $GF\parallel JI\parallel CE$.

Other than the free jet contribution to the density $n_w(X,Y,Z)$ at the surface, the corresponding contribution to the density at the surface from an inclined diffuse reflective surface is:

$$\frac{n_w\sqrt{RT_w}}{\sqrt{2\pi}}=n_jU_j\sin\alpha_0-n_jW_j\cos\alpha_0. \tag{3.1}$$

https://doi.org/10.4208/cicp.OA-2016-0165 Published online by Cambridge University Press

For a specular reflective surface, the contributions to the density from the true or virtual nozzles are identical:

$$n_w(s,\tau)=n_j(X,Y,Z). \tag{3.2}$$

Both relations are obtained by satisfying the non-penetration surface boundary condition.

There are two slip velocities for a diffuse reflective surface. One is along the surface inclination direction, the direction parallel to line DE in Fig. 1 and the other direction is along the "Y" direction, i.e., the direction parallel to line FI. The expressions are:

$$u_{s1}(s,\tau)=\frac{n_jU_j\cos\alpha_0+n_jW_j\sin\alpha_0}{n_w(s,\tau)+n_j},\qquad u_{s2}(s,\tau)=\frac{n_jV_j}{n_w(s,\tau)+n_j}. \tag{3.3}$$

The contribution from the diffuse plate surface to the velocity component along the plate tangential v-directions is zero because reflected particles evenly distribute their reflected velocity within a solid angle of 2π.

Correspondingly, there are two slip velocities along a specular reflective surface:

$$u_{s3}(s,\tau)=U_j\cos\alpha_0+W_j\sin\alpha_0,u_{s4}(s,\tau)=V_j. \tag{3.4}$$

The first slip velocity is along the inclined direction which is parallel to GF, and the latter is along the "Y" direction which is parallel to line FI.

Based on the gaskinetic theory, for a diffuse plate, the surface pressure coefficient at point $P(X,Y,Z)$ in the global coordinate system, or $P(s,\tau)$ in the local coordinate system, can be derived as:

$$\begin{aligned}C_{p,d}=&\frac{2}{n_0U_0^2}\sum_{i=j,w}n_i\left(\frac{\beta_i}{\pi}\right)^{3/2}\int_{\Omega_i}c_{n,i}^2e^{-\beta_i(u^2+v^2+w^2)}dudvdw\\=&\frac{2}{S_0^2}\frac{e^{-S_0^2}}{\sqrt{\pi}^3X^2}\int_0^{R_0}rdr\int_0^{2\pi}\frac{A_2}{Q^5}[\sin\alpha_0-B_1\cos\alpha_0]^2d\theta+\frac{\epsilon}{2S_0^2}\frac{n_w(s,\tau)}{n_0},\end{aligned} \tag{3.5}$$

where $B_1=(Z-r\sin\theta)/X$; "j" and "w" represent "jet" and "wall" correspondingly; $\beta_w=1/(2RT_w)$, $c_{n,j}=(u+U_0)\sin\alpha_0-w\cos\alpha_0$ and $c_{n,w}=u\sin\alpha_0-w\cos\alpha_0$ are the thermal velocity along the surface normal direction; and $\epsilon=T_w/T_0$ is the temperature ratio. It shall be reminded that at the plate surface, the pressure is defined along the normal direction, but at a flowfield point, the pressure is computed by averaging the components along the three directions. A helpful re-organization relation $u^2+v^2+w^2=(u+U_0)^2/Q^2+U_0^2-(u+U_0)U_0$ is used during the derivation.

For a diffuse flat surface, there are two friction forces along the plate surface. The friction coefficient related to the inclination direction, i.e., parallel to line FG is:

$$\begin{aligned}C_{f,\tau}=&\frac{2}{n_0U_0^2}\sum_{i=j,w}n_i\left(\frac{\beta_i}{\pi}\right)^{3/2}\int_{\Omega_i}c_{n,i}c_{\tau,i}e^{-\beta_i(u^2+v^2+w^2)}dudvdw\\=&\frac{2}{S_0^2}\frac{e^{-S_0^2}}{\sqrt{\pi}^3X^2}\int_0^{R_0}\frac{A_2}{Q^5}rdr\int_0^{2\pi}\left[\frac{1-B_1^2}{2}\sin2\alpha_0-B_1\cos2\alpha_0\right]d\theta,\end{aligned} \tag{3.6}$$

https://doi.org/10.4208/cicp.OA-2016-0165 Published online by Cambridge University Press

where $c_{\tau,j}=(u+U_0)\cos\alpha_0+w\sin\alpha_0$, $c_{\tau,w}=u\cos\alpha_0+w\sin\alpha_0$.

The other friction force is along the $v-$ or $Y-$ direction, parallel to line FI, is:

$$C_{f,s}=\frac{2}{n_0U_0^2}\sum_{i=j,w}n_i\left(\frac{\beta_i}{\pi}\right)^{3/2}\int_{\Omega_i}c_{n,i}c_{s,i}e^{-\beta_i(u^2+v^2+w^2)}dudvdw$$
$$=\frac{2}{S_0^2}\frac{e^{-S_0^2}}{\sqrt{\pi}^3X^2}\int_0^{R_0}\frac{A_2B_2}{Q^5}rdr\int_0^{2\pi}\left(\sin\alpha_0-B_1\cos\alpha_0\right)d\theta, \tag{3.7}$$

where $c_{s,j}=c_{s,w}=v$, and $B_2=(Y-r\cos\theta)/X$. It shall be emphasized that these two expressions share similarities.

The heat flux is along the direction normal to the plate, and the coefficient reads:

$$C_q=\frac{2}{n_0U_0^3}\sum_{i=j,w}n_i\left(\frac{\beta_i}{\pi}\right)^{3/2}\int_{\Omega_i}\frac{1}{2}c_{n,i}(c_{n,i}^2+c_{s,i}^2+c_{\tau,i}^2)e^{-\beta_i(u^2+v^2+w^2)}dudvdw$$
$$=\frac{1}{\sqrt{\pi}S_0^3}\left(\frac{e^{-S_0^2}}{\pi X^2}\int_0^{R_0}\frac{A_3}{Q^4}(\sin\alpha_0-B_1\cos\alpha_0)rdr\int_0^{2\pi}d\theta-\sqrt{\epsilon^3}\frac{n_w(s,\tau)}{n_0}\right), \tag{3.8}$$

where

$$A_3=\frac{\sqrt{\pi}}{4}[1+\mathrm{erf}(a)]e^{a^2}\left[2a^5+10a^3+\frac{15}{2}a\right]+\frac{a^4}{2}+\frac{9}{4}a^2+1, \tag{3.9}$$

where $a=S_0/Q$. As shown, the final plate surface expressions are complex and the plate temperature affects the surface coefficients.

For a specular surface, the shear stress and heat flux are zero due to the symmetry, and the surface pressure coefficient is simply two times the contribution from free jet to the surface:

$$C_{p,s}=\frac{4}{S_0^2}\frac{e^{-S_0^2}}{\sqrt{\pi}^3X^2}\int_0^{R_0}rdr\int_0^{2\pi}\frac{A_2}{Q^5}[\sin\alpha_0-B_1\cos\alpha_0]^2d\theta, \tag{3.10}$$

the plate temperature does not have any effects on the plate surface pressure coefficient.

4 Collisionless circular jet impingement on an inclined diffuse reflective plate

The problem and the thermal velocity integration domains for a point $P(X,Y,Z)$ between the nozzle and the plate are illustrated by Figs. 1 and 2. The contributions to the flowfield and surface properties are essentially from two sources, the free plume and the rectangular plate surface.

As mentioned in Section 3, due to the inclination relation, it is possible that none of the velocity components, $u-$, $v-$ and $w-$, are bounded, and this create a serious issue for the analysis. The solution is to perform proper velocity rotations from (u,v,w) to

https://doi.org/10.4208/cicp.OA-2016-0165 Published online by Cambridge University Press

(u_n,v,u_s), where the direction of u_n is pointing to the right down direction, as shown in Fig. 1. The direction for u_s is parallel to the plate surface, i.e., parallel to the direction of FI. With these notations, the three velocity unit vectors are:

$$u_n:(\sin\alpha_0,0,-\cos\alpha_0),\qquad v:(0,1,0),\qquad u_s:(\cos_0,0,\sin\alpha_0). \tag{4.1}$$

The velocity transformation relations are:

$$\begin{aligned} &u_n=u\sin\alpha_0-w\cos\alpha_0, \qquad u_s=u\cos\alpha_0+w\sin\alpha_0;\\ &u=u_n\sin\alpha_0+u_s\cos\alpha_0, \qquad w=u_s\sin\alpha_0-u_n\cos\alpha. \end{aligned} \tag{4.2}$$

A surface point (x,y,z) can also be represented with local coordinates on the flat plate surface, as (s,τ):

$$x=L+\tau\cos\alpha_0,\qquad y=s,\qquad z=\tau\sin\alpha_0. \tag{4.3}$$

The constitutive relation between location and velocity components can be extended by projecting vector from $P(X,Y,Z)$ in the flowfield to a point $p(s,\tau)$ on the plate, along the plate normal direction:

$$\frac{D_n}{u_n}=\frac{Y-s}{v}=\frac{D_s-\tau}{u_s}, \tag{4.4}$$

where

$$D_n=(X-L)\sin\alpha_0-Z\cos\alpha_0,\qquad D_s=(X-L)\cos\alpha_0+Z\sin\alpha_0; \tag{4.5}$$

by using the Jacobian relation, we have the following variable transformation:

$$dvdu_s=\frac{u_n^2}{D_n^2}d\tau ds \tag{4.6}$$

and the following velocity relations hold:

$$u^2+w^2=u_n^2+u_s^2, u^2+v^2+w^2=u_n^2Q_d^2, Q_d^2=1+\frac{(Y-s)^2}{D_n^2}+\frac{(D_s-\tau)^2}{D_n^2}. \tag{4.7}$$

From the gaskinetic theory, with two integration domains Ω_j and Ω_w shown in Fig. 2, the bulk properties at the flowfield point $P(X,Y,Z)$ are:

$$\begin{aligned} &\frac{n_d}{n_0}=\frac{1}{n_0}\sum_{i=j,w}\left(\frac{\beta_i}{\pi}\right)^{3/2}\int_{\Omega_i}n_ie^{-\beta_i(u^2+v^2+w^2)}dudvdw\\ &=\frac{e^{-S_0^2}}{X^2\sqrt{\pi}^3}\int_0^{R_0}\frac{1}{Q^3}rdr\int_0^{2\pi}A_0d\theta+\frac{1}{4\pi D_n^2}\int_{-H}^{H}d\tau\int_{-W}^{W}\frac{n_w}{n_0}\frac{ds}{Q_d^3}, \end{aligned} \tag{4.8}$$

$$\begin{aligned} &\frac{n_d}{n_0}\frac{U_d}{\sqrt{2RT_0}}=\frac{2}{n_0U_0^2}\sum_{i=j,w}\left(\frac{\beta_i}{\pi}\right)^{3/2}\int_{\Omega_i}n_iu_ie^{-\beta_i(u^2+v^2+w^2)}dudvdw\\ &=\frac{e^{-S_0^2}}{X^2\sqrt{\pi}^3}\int_0^{R_0}\frac{A_1r}{Q^4}dr\int_0^{2\pi}d\theta-\frac{\sqrt{\epsilon}}{2D_n^2\sqrt{\pi}^3}\int_{-H}^{H}d\tau\int_{-W}^{W}\frac{n_w}{n_0}\left(\sin\alpha_0+\frac{D_s-\tau}{D_n}\cos\alpha_0\right)\frac{ds}{Q_d^4}, \end{aligned} \tag{4.9}$$

https://doi.org/10.4208/cicp.OA-2016-0165 Published online by Cambridge University Press

where $u_j=u+U_0$ and $u_w=u$.

$$\frac{n_d}{n_0}\frac{V_d}{\sqrt{2RT_0}}=\frac{2}{n_0U_0^2}\sum_{i=j,w}\left(\frac{\beta_i}{\pi}\right)^{3/2}\int_{\Omega_i}n_i v e^{-\beta_i(u^2+v^2+w^2)}dudvdw$$
$$=\frac{e^{-S_0^2}}{X^2\sqrt{\pi}^3}\int_0^{R_0}\frac{A_1B_2r}{Q^4}dr\int_0^{2\pi}d\theta-\frac{\sqrt{\epsilon}}{2D_n^2\sqrt{\pi}^3}\int_{-H}^{H}d\tau\int_{-W}^{W}\frac{n_w}{n_0}\frac{Y-s}{D_n}\frac{ds}{Q_d^4}, \tag{4.10}$$

$$\frac{n_d}{n_0}\frac{W_d}{\sqrt{2RT_0}}=\frac{2}{n_0U_0^2}\sum_{i=j,w}\left(\frac{\beta_i}{\pi}\right)^{3/2}\int_{\Omega_i}n_i w e^{-\beta_i(u^2+v^2+w^2)}dudvdw$$
$$=\frac{e^{-S_0^2}}{X^2\sqrt{\pi}^3}\int_0^{R_0}\frac{A_1B_1r}{Q^4}dr\int_0^{2\pi}d\theta-\frac{\sqrt{\epsilon}}{2D_n^2\sqrt{\pi}^3}\int_{-H}^{H}d\tau\int_{-W}^{W}\frac{n_w}{n_0}\left(\frac{D_s-\tau}{D_n}\sin\alpha_0-\cos\alpha_0\right)\frac{ds}{Q_d^4}, \tag{4.11}$$

$$\frac{T_d}{T_0}=\frac{1}{3RT_0n_d}\sum_{i=j,w}\int_{\Omega_i}n_i\left[(u_i-U_d)^2+(v-V_d)^2+(w-W_d)^2\right]\sqrt{\frac{\beta_i}{\pi}}^3 e^{-\beta_i(u^2+v^2+w^2)}dudvdw$$
$$=\frac{2}{3}\frac{n_0}{n_d}\frac{e^{-S_0^2}}{X^2}\int_0^{R_0}\frac{rA_2}{Q^3}dr\int_0^{2\pi}d\theta-\frac{U_d^2+V_d^2+W_d^2}{3RT_0}+\frac{\epsilon}{4n_d\pi D_n^2}\int_{-H}^{H}\int_{-W}^{W}\frac{n_w d\tau ds}{Q_d^3}. \tag{4.12}$$

It shall be emphasized that during the derivations, the integrations over u_n shall be within$(-\infty,0)$, not $(0,+\infty)$ for those particles reflected back from the plate surface.

5 Collisionless circular jet impingement on an inclined specular reflective plate

The problem and the thermal velocity integration domains for a point $P(X,Y,Z)$ between the nozzle and the plate are illustrated by Figs. 3 and 4. The virtual nozzle has an inclined angle of $2\alpha_0-\pi/2$; hence, the treatment is quite similar to the diffuse plate scenario. The jet velocity components from the virtual nozzle are $(U_0\cos(2\alpha_0),0,U_0\sin(2\alpha_0))$. For convenience, we denote $p=u+U_0\cos(2\alpha_0)$, and $q=w+U_0\sin(2\alpha_0)$.

Similar velocity component rotations are performed, from (u,v,w) to (u_n,v,u_s), where u_n is pointing to the right down direction, as Fig. 3 illustrates. With these notations, the directions for the three velocity vectors are:

$$u_n:(-\cos2\alpha_0,0,-\sin2\alpha_0),\qquad v:(0,1,0),\qquad u_s:(\sin2\alpha_0,0,-\cos2\alpha_0), \tag{5.1}$$

and the transformation relations between the velocities are:

$$u_n=-q\sin2\alpha_0-p\cos2\alpha_0,\qquad u_s=-q\cos2\alpha_0+p\sin2\alpha_0; \tag{5.2}$$

https://doi.org/10.4208/cicp.OA-2016-0165 Published online by Cambridge University Press

a point on the virtual nozzle, (x,y,z), in a global coordinate system, can also be represented with local coordinates on the nozzle (r,θ):

$$x=L-L\cos 2\alpha_0+r\sin\theta\sin 2\alpha_0,\qquad y=r\cos\theta,\qquad z=-L\sin 2\alpha_0-r\sin\theta\cos 2\alpha_0. \tag{5.3}$$

The constitutive relation between locations and velocity components can be extended by projecting the vector from $P(X,Y,Z)$ to $p(r,\theta)$ along the three velocity directions:

$$\frac{E_1}{u_n}=\frac{Y-r\cos\theta}{v}=\frac{E_2-r\sin\theta}{u_s}, \tag{5.4}$$

$$E_1=(L-X)\cos 2\alpha_0-Z\sin 2\alpha_0-L,\qquad E_2=(X-L)\sin 2\alpha_0-Z\cos 2\alpha_0, \tag{5.5}$$

$$p=u_s\sin 2\alpha_0-u_n\cos 2\alpha_0,\qquad q=-u_s\cos 2\alpha_0-u_n\sin 2\alpha_0. \tag{5.6}$$

With the following velocity relations:

$$u^2+v^2+w^2=u_n^2+v^2+u_s^2+U_0^2+2U_0u_n,\qquad u_s=E_3u_n,\qquad v=E_4u_n, \tag{5.7}$$

$$E_3=\frac{E_2-r\sin\theta}{E_1},\qquad E_4=\frac{Y-r\cos\theta}{E_1}, \tag{5.8}$$

by using the Jacobian transformation, the integration over the velocity domain for the virtual nozzle can transfer to round nozzle surface coordinates:

$$dvdu_s=\frac{u_n^2}{E_1^2}rdrd\theta, \tag{5.9}$$

and the final expressions for the bulk flowfield properties are:

$$\begin{aligned}\frac{n_s(X,Y,Z)}{n_0}&=\left(\frac{\beta_0}{\pi}\right)^{3/2}\int_{\Omega_j+\Omega_s}e^{-\beta_0(u^2+v^2+w^2)}dudvdw\\&=\frac{e^{-S_0^2}}{\sqrt{\pi}^3}\int_0^{R_0}\left(\frac{A_0}{X^2Q^3}+\frac{A_0(a_n)}{E_1^2Q_n^3}\right)rdr\int_0^{2\pi}d\theta,\end{aligned} \tag{5.10}$$

$$Q_n^2=1+E_3^2+E_4^2,a_n=S_0/Q_n, \tag{5.11}$$

$$\begin{aligned}\frac{n_s}{n_0}\frac{U_s}{\sqrt{2RT_0}}&=\frac{1}{\sqrt{2RT_0}}\sum_{i=j,s}\left(\frac{\beta_0}{\pi}\right)^{3/2}\int_{\Omega_i}u_ie^{-\beta_0(u^2+v^2+w^2)}dudvdw\\&=\frac{e^{-S_0^2}}{\sqrt{\pi}^3}\int_0^{R_0}\left(\frac{A_1}{X^2Q^4}-\frac{E_5A_1(a_n)}{E_1^2Q_n^4}\right)rdr\int_0^{2\pi}d\theta,\end{aligned} \tag{5.12}$$

https://doi.org/10.4208/cicp.OA-2016-0165 Published online by Cambridge University Press

where $u_j=u+U_0$, $u_s=u+U_0\cos2\alpha_0$, and $E_5=E_3\sin2\alpha_0-\cos2\alpha_0$.

$$\frac{n_s}{n_0}\frac{V_s}{\sqrt{2RT_0}}=\frac{1}{\sqrt{2RT_0}}\left(\frac{\beta_0}{\pi}\right)^{3/2}\int_{\Omega_j+\Omega_s}ve^{-\beta_0(u^2+v^2+w^2)}dudvdw$$
$$=\frac{e^{-S_0^2}}{\sqrt{\pi}^3}\int_0^{R_0}\left(\frac{A_1B_2}{X^2Q^4}-\frac{E_4A_1(a_n)}{E_1^2Q_n^4}\right)rdr\int_0^{2\pi}d\theta, \tag{5.13}$$

$$\frac{n_s}{n_0}\frac{W_s}{\sqrt{2RT_0}}=\frac{1}{\sqrt{2RT_0}}\sum_{i=j,s}\left(\frac{\beta_0}{\pi}\right)^{3/2}\int_{\Omega_i}w_ie^{-\beta_0(u^2+v^2+w^2)}dudvdw$$
$$=\frac{e^{-S_0^2}}{\sqrt{\pi}^3}\int_0^{R_0}\left(\frac{A_1B_1}{X^2Q^4}+\frac{E_6A_1(a_n)}{E_1^2Q_n^4}\right)rdr\int_0^{2\pi}d\theta, \tag{5.14}$$

where $w_j=w$, $w_s=w+U_0\sin2\alpha_0$ and $E_6=\sin2\alpha_0+E_3\cos2\alpha_0$.

$$\frac{T_s}{T_0}=\frac{1}{3RT_0n_s}\sum_{i=j,s}\int_{\Omega_i}n_0\left[(u_i-U_s)^2+(v-V_s)^2+(w_i-W_s)^2\right]\sqrt{\frac{\beta_0}{\pi}}^3e^{-\beta_0(u^2+v^2+w^2)}dudvdw$$
$$=\frac{2}{3}\frac{n_0}{n_s}\frac{e^{-S_0^2}}{\sqrt{\pi}^3}\int_0^{R_0}\left(\frac{A_2}{X^2Q^3}+\frac{A_2(a_n)}{E_1^2Q_n^3}\right)rdr\int_0^{2\pi}d\theta-\frac{U_s^2+V_s^2+W_s^2}{3RT_0}. \tag{5.15}$$

As shown, there are strong connections between contributions from the real and virtual nozzles.

6 Validations

Most of the above analytical solutions and expressions involve complex integrations which need numerical evaluations with a computer. Due to their complex expressions, numerical simulations must be performed to validate them. In this work, all DSMC [21] simulations are performed with a special package, GRASP [25], which is a general purpose particle simulation package, with special object-oriented programming styles and software engineering design patterns. It is assumed that the test gas is Argon, and the nozzle diameter D = 1 m. The center-to-center distance from the nozzle exit to the plate, L, is chosen as four times of the nozzle diameter. Both the plate semi-length W_0 and the semi-height H_0 are set as the same length of L. The exit speed ratio is $S_0=2.0$, the exit gas temperature is 200 Kelvin, and the plate surface temperature is set as 300 Kelvin.

The simulation domain is three-dimensional, with a truncated pyramid shape which can be conveniently perceived with Fig. 1. An inlet boundary condition to the simulation domain is used to represent the round nozzle exit at the left side; a rectangular diffuse or specular plate with surface boundary conditions is set at the right end of the simulation domain at the opposite side to the jet nozzle; all the remaining boundary conditions for the simulation domain are set as outlet. When reflected molecules reach the outlet, or

https://doi.org/10.4208/cicp.OA-2016-0165 Published online by Cambridge University Press

inlet (i.e. nozzle exit), they are removed from simulations. Different plate inclination angles may be adopted, and the scenario of 90° is used to examine the symmetry patterns in the solutions. For the scenario of $\alpha_0 = 60°$, a total of about 11 thousand triangular meshes are used to represent the simulation outer boundaries, and there are about 210 thousand tetrahedral cells in the simulation domain. On the plate surface and at locations closer to the plate surface, denser meshes are used to obtain better resolutions. In the final steady flow stage, there are about two million particles in the DSMC simulations for the a diffuse plate situation, the number for the specular plate scenario is slightly different.

6.1 Contributions to the surface number density by the plate, and slip velocities

Figs. 5 and 6 show the contributions to the surface number density by a diffuse or specular reflective flat plate, respectively. They correspond to Eqs. (3.1) and (3.2). The parameters are: $S_0 = 2.0$, $T_w/T_0 = 1.5$, and $\alpha = 60°$. Parameters s and τ represent the local coordinates on the plate. The contour values are normalized by the free jet number density. With these parameters, the specular plate yields lower density, indicating that it is more effective to scatter off gas molecules. These two figures illustrate that the highest number densities may not happen at the plate center due to the existence of the inclination angle. The density levels off from the plate center towards the plate edges.

Figs. 7 and 8 show the slip velocities along the inclination direction. They correspond to Eq. (3.3). They illustrate that: 1) the slip happens at all locations, except there are two zero-value lines which are slightly curved. Along those two lines, the slip velocities along the τ direction are zero, but the slip velocities along the s direction may not be zero; 2) there is a true stagnation point located at these two curves below the plate center, due

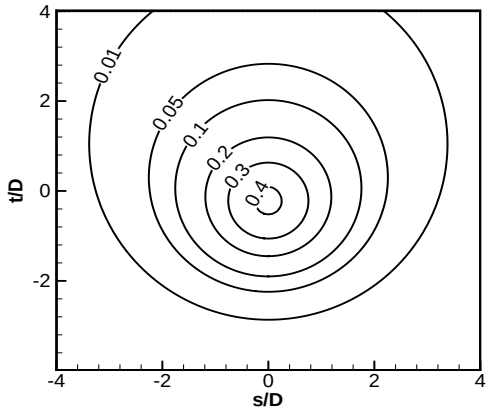


Figure 5: Diffuse Plate Surface Number Density Contributed From the Plate Blockage, $S_0 = 2.0$, $T_w/T_0 = 1.5$, $\alpha_0 = 60°$, $L/D = 4$.

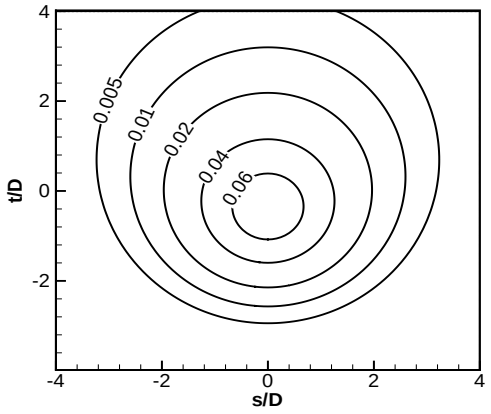


Figure 6: Specular plate surface number density contributed from the plate blockage, $S_0 = 2.0$, $\alpha_0 = 60°$, $T_w/T_0 = 1.5$, $L/D = 4$.

https://doi.org/10.4208/cicp.OA-2016-0165 Published online by Cambridge University Press

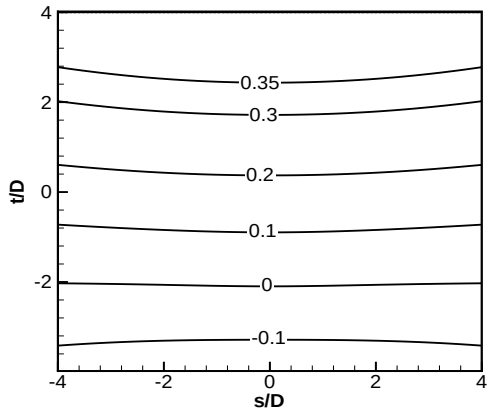


Figure 7: Diffuse plate surface slip velocity along the inclination direction, $S_0 = 2.0$, $T_w/T_0 = 1.5$, $\alpha_0 = 60^\circ$, $L/D = 4$.

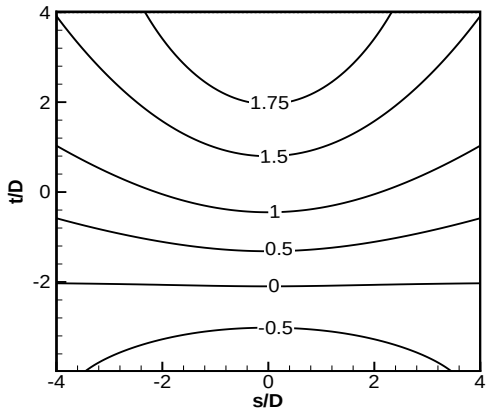


Figure 8: Specular plate surface slip velocity along the inclination direction, $S_0 = 2.0$, $\alpha_0 = 60^\circ$, $T_w/T_0 = 1.5$, $L/D = 4$.

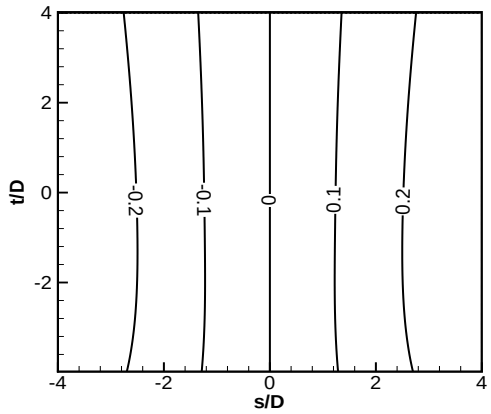


Figure 9: Diffuse plate surface slip velocity along the horizontal direction, $S_0 = 2.0$, $T_w/T_0 = 1.5$, $\alpha_0 = 60^\circ$, $L/D = 4$.

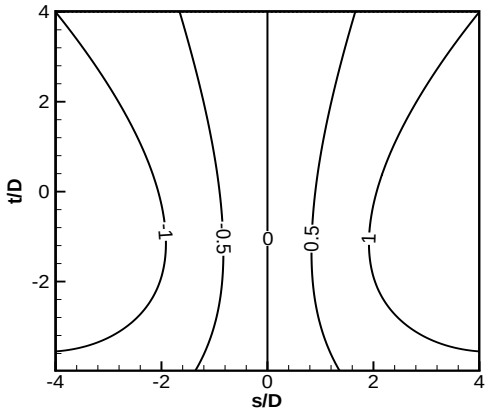


Figure 10: Specular plate surface slip velocity along the horizontal direction, $S_0 = 2.0$, $\alpha_0 = 60^\circ$, $T_w/T_0 = 1.5$, $L/D = 4$.

to the plate inclination effect; 3) the symmetry patterns from the left to the right side are evident; 4) along the centerline $s = 0$, the slip velocity gradients are the largest; 5) for the specular reflective surface, the slip velocity is several times larger than that for the diffuse plate surface, indicating the specular plate is more "slippy" at the collisionless flow limit, and it is more effective to scatter particles off. The above results are obtained with a specific parameter combination, and the conclusions may be generally valid for other parameter combinations.

Figs. 9 and 10 show the surface slip velocities but along the horizontal direction. They

https://doi.org/10.4208/cicp.OA-2016-0165 Published online by Cambridge University Press

correspond to Eqs. (3.4). The curves at the left sides with negative values represent slip velocities to the left, while those curves with positive values at the right side represent slip velocity to the right. The curves for the diffuse plate scenario are relatively straight with smaller curvatures; by comparison, the curves for the specular reflective plate have larger velocities, bigger curvatures and gradients.

6.2 Flowfield patterns

The next ten figures are the flowfield results. The simulation domain and the length scales are normalized by the nozzle diameter. The gas speed ratio at the nozzle exit is $S_0=2.0$, and the plate inclination angle is 60°. The temperature ratio is $T_w/T_0=1.5$. This temperature ratio does not have any effects on the flowfield results related to a specular plate. For the scalar properties in the specular reflective plate scenario, including the density, pressure and temperature results, there are symmetric patterns at the surface, i.e., $\partial/\partial n=0$ at the plate surface. For the velocity components, due to the existence of velocity slips along the plate surface, these symmetric patterns do not exist. The simulations are three-dimensional, and those flowfield results in the next ten figures are obtained from the cut-through plane with $Y=0$. These results are the most complex due to the inclination angle.

Figs. 11 and 12 are the density contours. There are appreciable differences for the situations of a diffuse or a specular reflective plate. For example, at the upper region, there are relatively smaller values than the corresponding lower portion, because more gas flows away from the plate via that region. Along the centerline $Z=0$, Fig. 11 indicates the density at the impingement center may have a value larger than 0.2, while for the specular plate impingement center, this value may be much smaller than 0.2. This

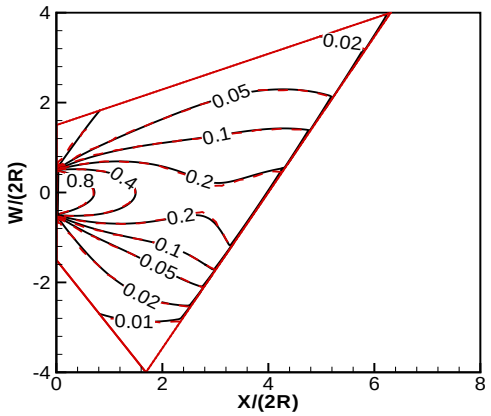


Figure 11: Diffuse plate: density contours, $S_0=2.0$, $T_w/T_0=1.5$, $\alpha_0=60^\circ$, $L/D=4$. Solid: DSMC, dashed: analytical.

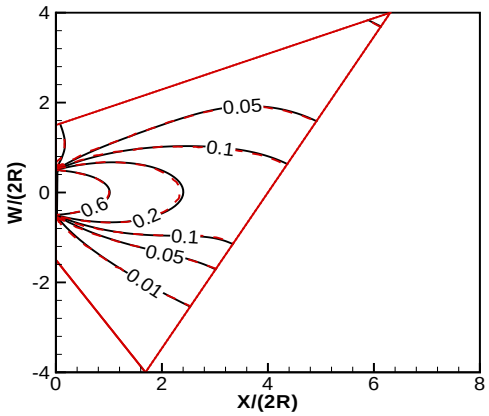


Figure 12: Specular plate: density contours, $S_0=2.0$, $\alpha_0=60^\circ$, $T_w/T_0=1.5$, $L/D=4$. Solid: DSMC, dashed: analytical.

https://doi.org/10.4208/cicp.OA-2016-0165 Published online by Cambridge University Press

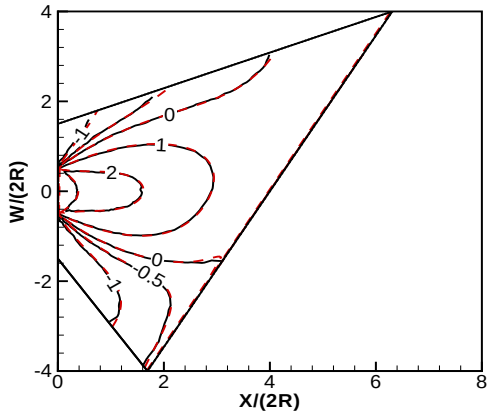


Figure 13: Diffuse plate: u-velocity component contours, S_0=2.0, T_w/T_0=1.5, α_0=60°, L/D=4. Solid: DSMC, dashed: analytical.

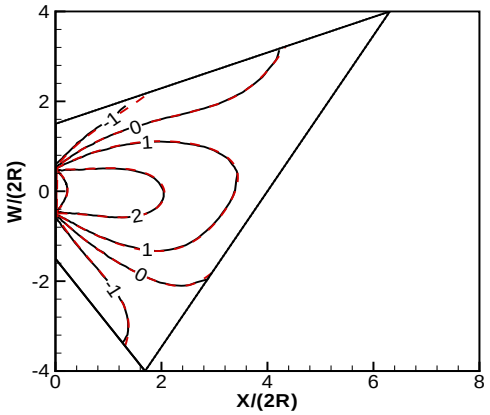


Figure 14: Specular plate: u-velocity component contours, S_0=2.0, α_0=60°, T_w/T_0=1.5, L/D=4. Solid: DSMC, dashed: analytical.

result indicates that the specular plate is much more effective to scatter off molecules. This is understandable because for a diffuse reflective plate, after reflections, particles have larger opportunities to stay around the plate because they have equal opportunity to scatter along any direction. However, for a specular reflective plate, the reflection angle is scattered exactly. The closer to the plate ends, and the larger change the particle has to leave the domain. This explanation is plausible for these parameters, whether it is generally valid needs to be tested. For example, the plate surface temperature has effects on the velocities of reflected particles, but it has no effects for the specular reflective surface. Different flowfield patterns may appear with different temperature ratio.

Figs. 13 and 14 show the u-velocity components. There are negative values in both figures, indicating a significant amount of particles moving backward. Another interesting fact is at the central region, the specular plate has much larger values: for example, the contour lines with value 1.0. For both scenarios, the amount of particles flowing to the plate at the right side is the same, a natural explanation is, for a specular plate, there are less particles reflected back along the centerline.

Figs. 15 and 16 show the velocity components along the inclination direction. By comparing these two figures, we conclude that the specular reflective plate scenario has more particles scattered upwards, and there are more complex patterns at the bottom side. The nozzle exit lips are singularity points with rapid changes. The flow fields are divided clearly into two streams flowing upwards and downwards, respectively. Interesting patterns emerge with zero-value contour lines, forming a zone where molecules flow downwards. This means that on average molecules move upwards there. This fact can be explained with the plate inclination and the finite size nozzle.

Figs. 17 and 18 show the temperature contours for a diffuse or a specular plate. The temperature ratio for the specular reflective plate scenario does not have any effects on

https://doi.org/10.4208/cicp.OA-2016-0165 Published online by Cambridge University Press

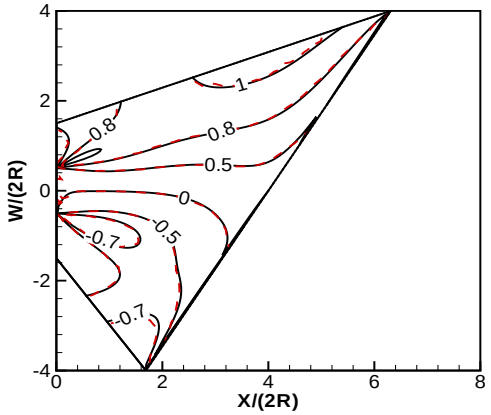


Figure 15: Diffuse plate: w-velocity component contours, S_0=2.0, T_w/T_0=1.5, α_0=60°, L/D=4. Solid: DSMC, dashed: analytical.

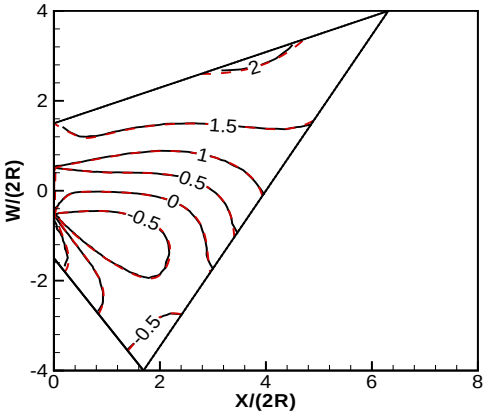


Figure 16: Specular plate: w-velocity component contours, S_0=2.0, α_0=60°, T_w/T_0=1.5, L/D=4. Solid: DSMC, dashed: analytical.

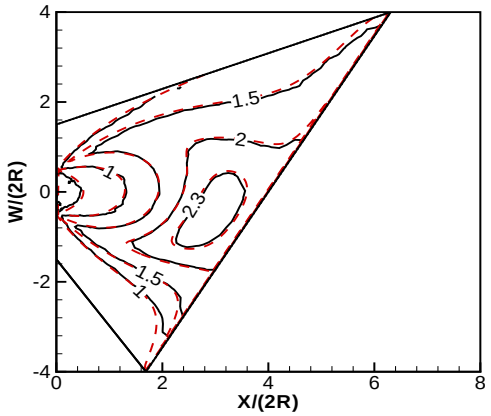


Figure 17: Diffuse plate: temperature contours, $S_0=2.0$, $T_w/T_0=1.5$, $\alpha_0=60°$, $L/D=4$. Solid: DSMC, dashed: analytical.

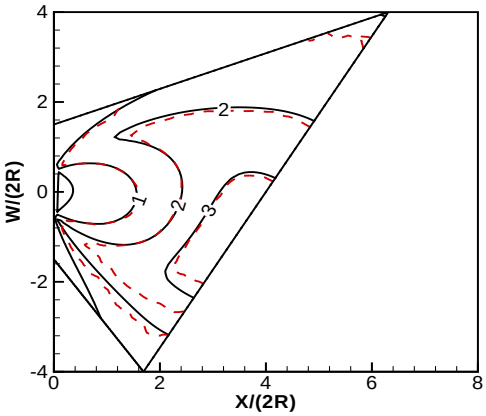


Figure 18: Specular plate: temperature contours, $S_0=2.0$, $\alpha_0=60°$, $T_w/T_0=1.5$, $L/D=4$. Solid: DSMC, dashed: analytical.

the temperature contours, and it is unexpected to have many flowfield feature changes. For the diffuse reflective plate situation, a hot or cold plate may create direct effects on the temperature fields. Due to the virtual nozzle, the temperature patterns are symmetric at the specular plate surface. The temperature values around the plate have larger values, most likely due to more evenly mixing at that region. For a diffuse plate, the locations and values for the highest temperature may vary. Almost no results in the literature by other researchers demonstrate the temperature ratio effects. Because temperature is a comprehensive result involving density and velocity components, it is challenging to obtain more accurate results.

https://doi.org/10.4208/cicp.OA-2016-0165 Published online by Cambridge University Press

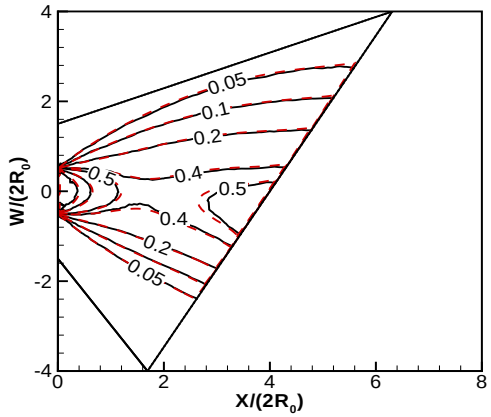


Figure 19: Diffuse plate: pressure contours, $S_0=2.0$, $T_w/T_0=1.5$, $\alpha_0=60^\circ$, $L/D=4$. Solid: DSMC, dashed: analytical.

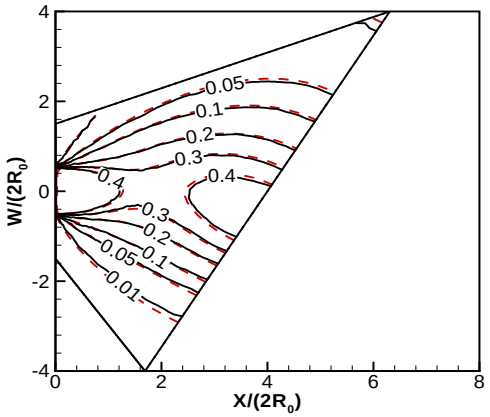


Figure 20: Specular plate: pressure contours, $S_0=2.0$, $\alpha_0=60^\circ$, $T_w/T_0=1.5$, $L/D=4$. Solid: DSMC, dashed: analytical.

Figs. 19 and 20 compare the pressure contours within the plane $Y=0$. For many engineering problems, especially for space engineering, the pressure distributions are of special interest because they create force and moment loads on the plate. The computation of pressure is straightforward by using the equation of state. These two figures show that the pressure increases in front of the plate due to the blockage effects, and there are symmetric patterns about the plate for the specular reflective scenario. In general, the pressure contours show better agreement than the corresponding temperature contours, probably because the density factor is partially removed from the expression for pressure.

6.3 Surface properties

For many engineering applications, the surface properties are of critical interest. These properties include pressure, friction, and heat coefficients. Different from the flowfield properties, which may be affected by the plate shape and size, the surface properties are solely determined by properties at the nozzle exit and the local plate surface point.

Figs. 21 and 22 show the coefficients for surface pressure. In these two figures, local coordinates along the horizontal and inclined direction are adopted. The symmetric patterns from the left to the right are evident, and for this parameter combination, the specular reflective plate scenario has a slightly higher value at the impingement center.

Figs. 23 and 24 are the shear stress coefficients along the inclination and horizontal directions for a diffuse reflective plate. Fig. 23 indicates the major portion of gas flows upwards with positive friction coefficients, and only a small portion flows downwards with negative friction coefficients. There is a stagnation line with zero shear stress along the inclination direction, indicating flows can separate along that line. Fig. 24 shows flow has the same opportunity to leave the plate from the left and right sides. There is also

https://doi.org/10.4208/cicp.OA-2016-0165 Published online by Cambridge University Press

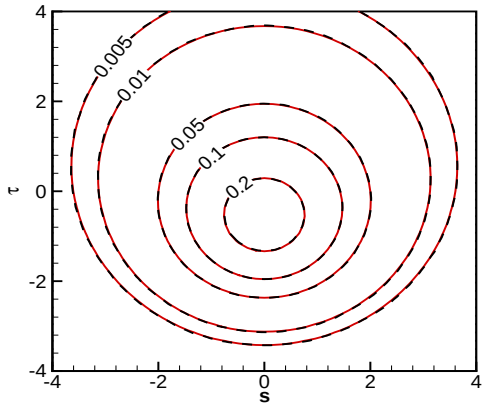


Figure 21: Diffuse plate surface pressure distributions, $S_0=2.0$, $T_w/T_0=1.5$, $\alpha_0=60°$, $L/D=4$. Plate lengths are normalized by the nozzle diameter. Solid: analytical, dashed: DSMC.

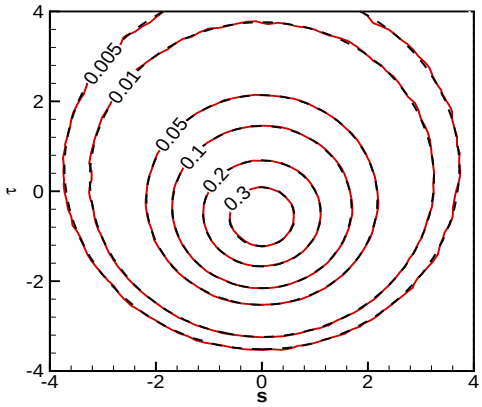


Figure 22: Specular plate surface pressure distributions, $S_0=2.0$, $\alpha_0=60°$, $T_w/T_0=1.5$, $L/D=4$. Plate lengths are normalized by the nozzle diameter. Solid: analytical, dashed: DSMC.

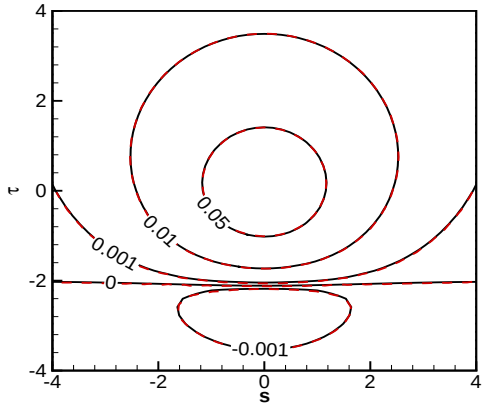


Figure 23: Diffuse plate surface friction distributions, $C_{f,\tau}$, along the inclination direction, S_0=2.0, $T_w/T_0=1.5$, $\alpha_0=60°$, $L/D=4$. Plate lengths are normalized by the nozzle diameter. Solid: analytical, dashed: DSMC.

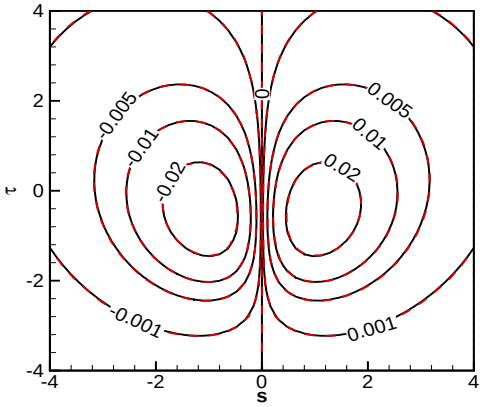


Figure 24: Diffuse plate surface friction distributions, $C_{f,s}$, along the horizontal direction, S_0=2.0, $T_w/T_0=1.5$, $\alpha_0=60°$, $L/D=4$. Plate lengths are normalized by the nozzle diameter. Solid: analytical, dashed: DSMC.

another straight zero-value line.

Fig. 25 shows the heat flux distributions at a diffuse reflective plate. At the impingement center, the heat flux reaches the highest value. For a specular reflective plate surface, the shear stress is zero because there is no moment change along the two tangent directions. The heat flux coefficient is also zero, because the heat flux into and out of the plate surface cancel.

https://doi.org/10.4208/cicp.OA-2016-0165 Published online by Cambridge University Press

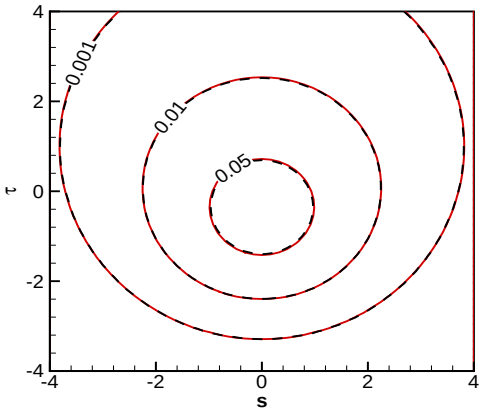


Figure 25: Diffuse plate surface heat flux distributions, $S_0=2.0$, $T_w/T_0=1.5$, $\alpha_0=60°$, $L/D=4$. Plate lengths are normalized by the nozzle diameter. Solid: analytical, dashed: DSMC.

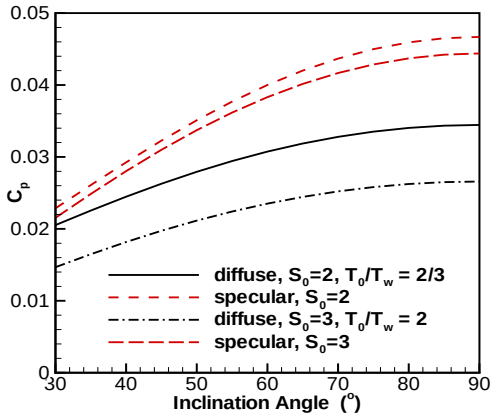


Figure 26: Inclination angle effects on averaged C_P, $L/D=4$.

The validations of flowfield and surface properties offer us solid foundations to proceed computation on the global or average loads on the whole plate. These loads include force, moment, torque, heat flux, and the center-to-center distance from the moment to the plate. These five averaged properties are named as C_P, C_{F1}, C_Q, C_M, and S_{cc}. Because the plate setup is symmetric, the total shear stress along the horizontal direction (y axis) is zero. However, as shown in this paper, the object surface and the nozzle can have any geometric shape. Hence, in general the shear stress coefficient, C_{F2} can also be computed with the expressions obtained in this study. These five properties are defined as follows:

$$C_P=\int_p C_p(s,\tau)dsd\tau/(4W_0H_0),\quad C_F=\int_p C_{f,\tau}(s,\tau)dsd\tau/(4W_0H_0),$$
$$C_Q=\int_p C_q(s,\tau)dsd\tau/(4W_0H_0),\quad C_M=\int_p \tau C_p(s,\tau)dsd\tau/(8W_0H_0^2),S_{cc}=C_M/C_P,\qquad (6.1)$$

where subscript "$_p$" means the integration domain is over the whole plate surface.

6.4 Inclination angle effects on the averaged surface properties

Fig. 26 illustrates inclination angle effects on C_P. In general, the averaged pressure increases monotonically as the plate inclination angle increases. It is difficult to declare whether a diffuse or a specular reflective surface may have a higher averaged pressure. With the same plate inclination angle, higher speed ratio S_0 may create lower pressure coefficients, because the expressions for the pressure coefficients contain a factor of $1/S_0^2$ factor in the denominator. A hotter plate gives particles larger reflected thermal velocities. As such, the pressure coefficient is higher, if other parameters remain unchanged.

https://doi.org/10.4208/cicp.OA-2016-0165 Published online by Cambridge University Press

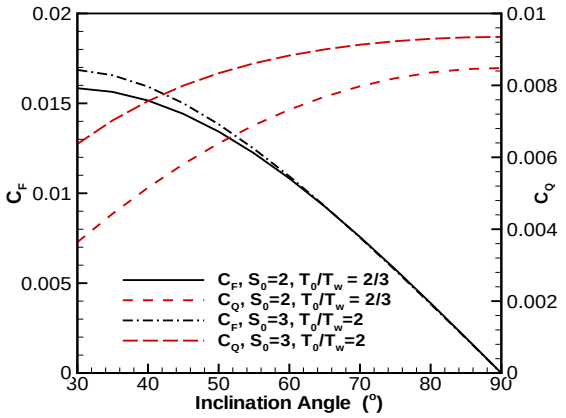


Figure 27: Inclination angle effects on averaged $C_{F,\tau}$ and C_Q, diffuse plate, $L/D=4$.

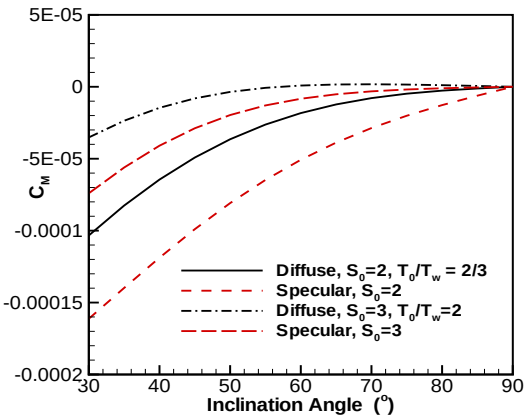


Figure 28: Inclination angle effects on C_M, $L/D=4$.

Fig. 27 shows the inclination effects on C_F along the inclined direction and heat flux over a diffuse reflective surface. It demonstrates that as the inclination angle increases, the friction coefficient diminishes because shear stress at the upper and lower parts of the plate balance and cancel each other. By comparison, the heat flux coefficient increases with larger plate inclination angles. When the plate is perpendicular to the jet, i.e., $\alpha_0 = 90^\circ$, the friction is zero and the heat load becomes maximum. For the other shear stress coefficient along the "y" direction, it is zero due to the symmetry of current setup. By definition, the friction and heat flux over a specular plate surface are always zero.

Fig. 28 shows the moment coefficient along the plate surface. As the inclination angle increases, the moment magnitude approaches to zero due to balanced pressure distributions and the moment from the top and bottom parts cancel. It is difficult to conclude whether the specular or the diffuse reflective plate scenario may have a larger moment coefficient. Fig. 29 shows the surface center-to-center distance between the plate and the moment, and the profiles are similar to those in Fig. 28. When the plate is perpendicular to the jet, the moment to the plate surface center is zero.

6.5 Speed ratio effects on the averaged surface properties

For many applications, the exit speed ratio effects on the plate surface are of major concerns. Fig. 30 shows the averaged pressure coefficients. As the exit speed ratio increases, the profiles decrease quickly. As the speed ratio increases to values, e.g. $S_0 = 10.$, the curves approach to a plateau with slow dropping speeds, and the incoming gas flow effects become dominant. Fig. 31 shows the exit speed ratio effects on the averaged friction and heat flux. Initially S_0 has appreciable effects, e.g., when $S_0 < 2$, but after a certain value, the curves level off. All those curves have the same asymptote values of zero due

https://doi.org/10.4208/cicp.OA-2016-0165 Published online by Cambridge University Press

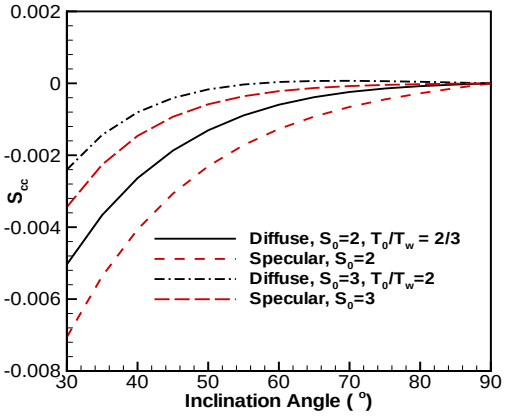


Figure 29: Inclination angle effects on S_{cc}, $L/D=4$.

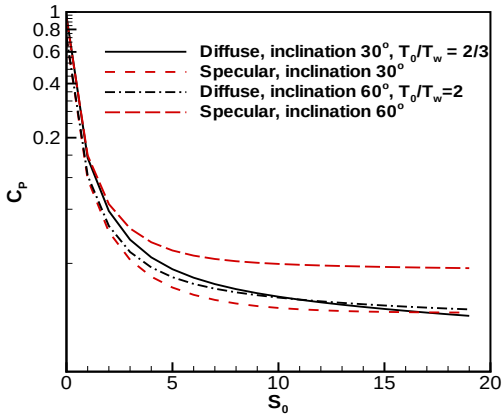


Figure 30: S_0 effects on averaged C_P, $L/D=4$.

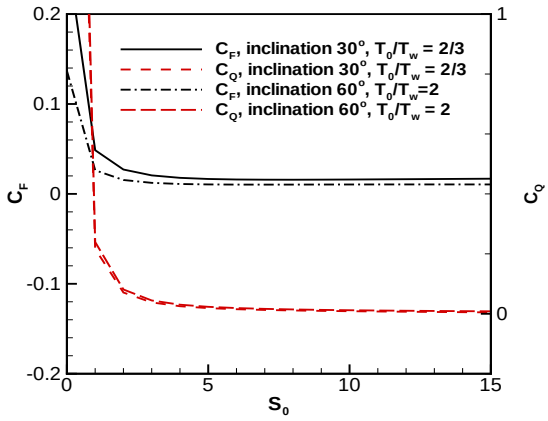


Figure 31: S_0 effects on averaged $C_{F,\tau}$ and C_Q, $L/D=4$.

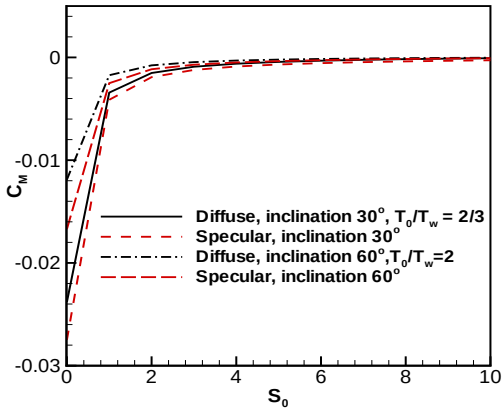


Figure 32: S_0 effects on averaged moment coefficients, C_M, $L/D=4$.

to the S_0^2 and S_0^3 factors in the dominator, and the heat flux coefficient decreases much faster. Figs. 32 and 33 show the averaged moment coefficient and the distance from the force center to the plate center. The same asymptote values of zero are evident. The negative values indicate that the force center locates at the lower part of the plate.

6.6 Temperature ratio effects on the averaged surface properties

Fig. 34 shows the T_w/T_0 ratio effects on C_P. For a specular plate, there is no moment exchange between a particle and the surface; hence, the pressure coefficient is not affected by the temperature ratio, and the curves are simply straight lines. For a diffuse plate surface, with a hotter surface, the reflected particles have larger reflected thermal velocities,

https://doi.org/10.4208/cicp.OA-2016-0165 Published online by Cambridge University Press

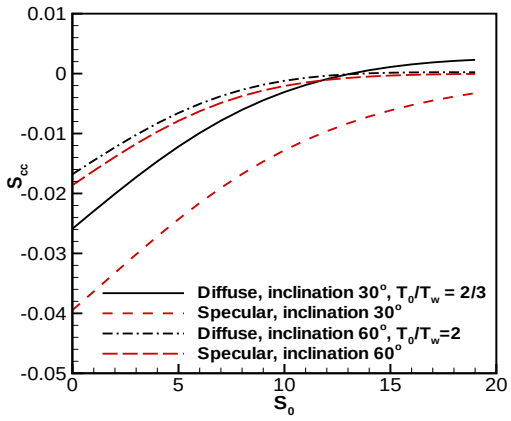


Figure 33: S_0 effects on averaged S_{cc}, $L/D=4$.

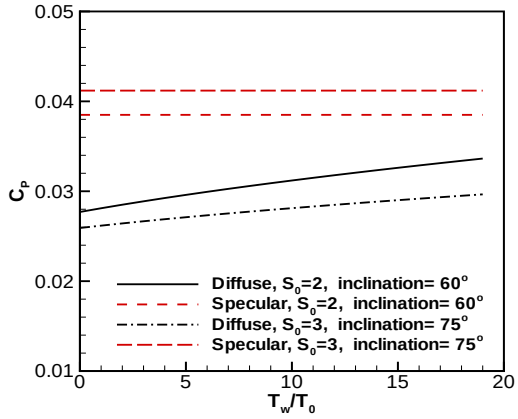


Figure 34: Temperature ratio effects on C_P, $L/D=4$.

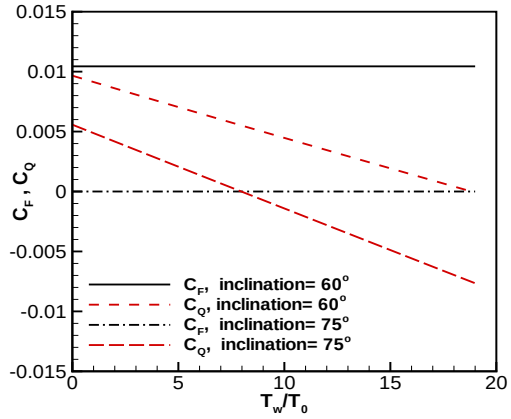


Figure 35: Temperature ratio effects on $C_{F,\tau}$ and C_Q, $S_0=2$, $L/D=4$, diffuse plate.

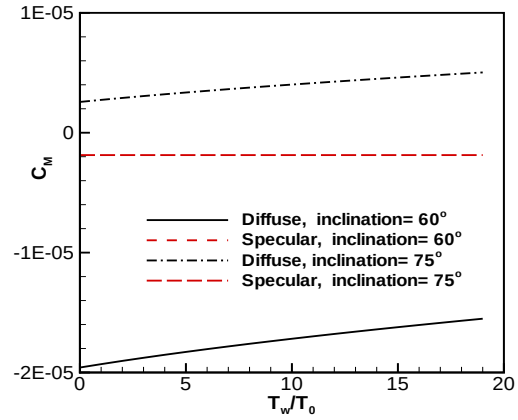


Figure 36: Temperature ratio effects on C_M, $S_0=2$, $L/D=4$.

and the pressure coefficient becomes larger. A larger pressure ratio leads to larger averaged pressure coefficient. Fig. 35 shows the diffuse surface average friction and heat flux, C_F and C_Q. The formula for friction distribution, Eq. (3.6), contains a temperature ratio; however, when it is integrated out to compute C_F, the temperature ratio almost has no effect on the shear stress. With a larger inclination angle, most friction force cancels and the net friction force is closer to zero. As the temperature ratio increases, the heat flux from the plate to the flowfield becomes dominant. Figs. 36 and 37 show the temperature ratio effects on the C_M and S_{cc}. A specular plate, no matter it is cold or hot, does not have any effects on the moment; as such, the curves are straight lines without any variations.

https://doi.org/10.4208/cicp.OA-2016-0165 Published online by Cambridge University Press

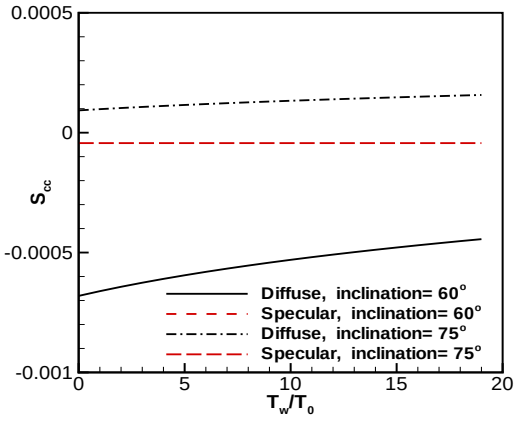


Figure 37: Temperature ratio effects S_{cc}, $S_0=2$, $L/D=4$.

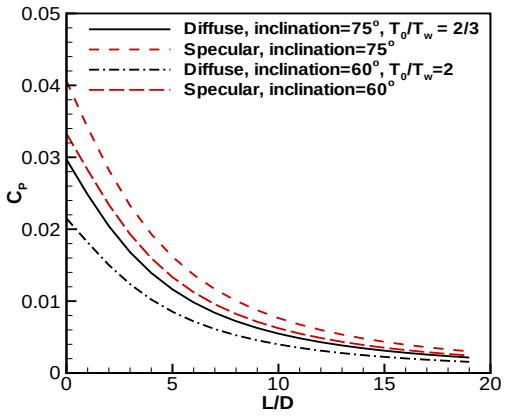


Figure 38: Length ratio L/D effects on C_P, $S_0=2$, $L/D=4$.

For a diffuse reflective plate, those reflected particles have larger thermal velocities at a hotter surface, and C_M and S_{cc} change with the same trends.

6.7 Distance ratio effects on the averaged surface properties

Fig. 38 shows the influences by the center-to-center distance from the plate to nozzle exit on C_P. No matter if the plate is diffuse or specular reflective, the pressure coefficients continue to decrease as the distance ratio increases, indicating that the pressure force becomes weaker. This can be explained with a decreasing solid angle subtended between the plate edges and the nozzle exit. A larger inclination angle and a hotter surface may both increase the pressure force. For the specular reflective surface, only the inclination angle may contribute to the surface pressure. Fig. 39 shows the length ratio effects on shear stress (along the plate inclination direction) and the surface heat flux coefficients along a diffuse reflective plate. The temperature ratio does not affect the surface slip velocity along a diffuse plate, but does affect the temperature jump and therefore the heat flux. The inclinations affect both the surface slip velocity and surface density contributed from the plate; hence, their effects can be quite appreciable. Figs. 40 and 41 show the corresponding moment load coefficients, C_M, and the distance between the force center to the plate center, S_{cc}. Because the friction forces are parallel to the plate surface, they do not contribute to the moment on the plate. These two figures illustrate that a larger inclination angle leads to smaller C_M and S_{cc}. With an inclination angle, the moment center locates at the lower part of the plate. However, the moment and center do not vary monotonically, and both have largest magnitudes at a specific L/D value. This fact may relate to the finite size of the nozzle. Even though at the farfield the values approach to zero, these two figures clearly illustrate that, within a certain distance from the nozzle, quite simple assumptions may be inappropriate.

https://doi.org/10.4208/cicp.OA-2016-0165 Published online by Cambridge University Press

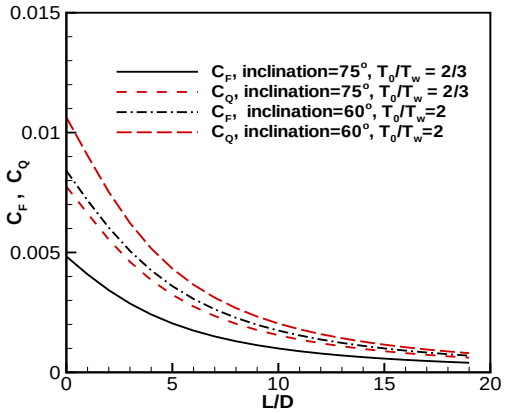


Figure 39: Length ratio L/D on averaged $C_{F,\tau}$ and C_Q, along a diffuse reflective plate, $S_0=2$.

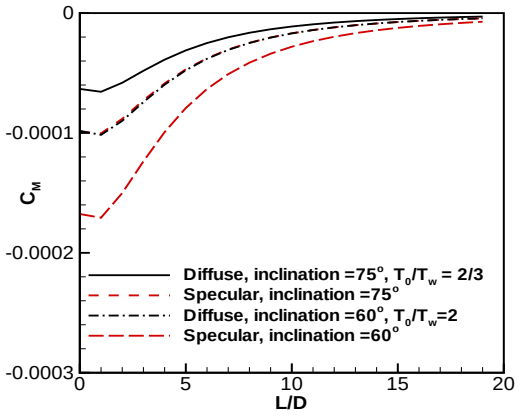


Figure 40: Length ratio L/D on C_M, $S_0=2$.

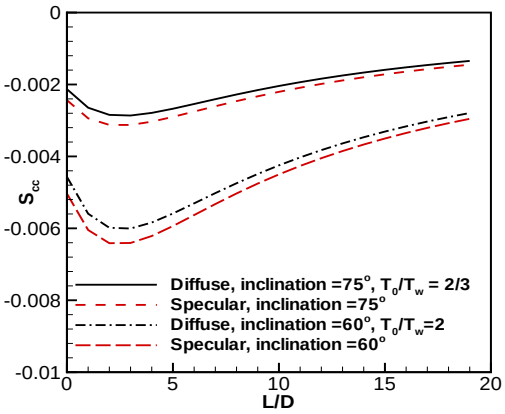


Figure 41: Length ratio L/D effects on S_{cc}, $S_0=2$.

7 Conclusions

In this paper, two fundamental problems of collisionless jet flows from a circular exit and jet impingement on an inclined diffuse or specular reflective flat plate are investigated. The fundamental assumptions are collisionless flows and the Maxwellian VDF distributions at the nozzle exit and the diffuse plate surface. Several fundamental relations among geometry-locations and velocity-directions are identified and used, simplifying integration results. Because the derivation processes are complex and lengthy, several crucial steps, such as the starting points for each expression, are kept in this paper to help interested readers understand the methods. The new formulas for flowfield properties, including number density, velocity, temperature, and pressure are presented for these two fundamental problems; surface properties such as pressure, shear stress, heat

https://doi.org/10.4208/cicp.OA-2016-0165 Published online by Cambridge University Press

flux, and slip velocity components are provided as well. Further, effects from different ratios on the total force, heat loads, moment, and distances from the moment center to the plate center are discussed. Several DSMC simulations are performed to validate these analytical solutions, and essentially identical agreement is observed.

The new solutions are complex, and involve geometry ratios, speed velocity ratio, and a temperature ratio. They are the counterpart solutions to the continuum gaseous jet and jet impingement problems, and offer us new insights to these fundamental problems. DSMC simulation can provide more accurate results with a consideration of collision effects; however, the simulations bury physics in a huge amount of numbers. Also, the evaluation of these formulas are quite fast which may only require tens of seconds; by comparison, the DSMC simulations in this work took several days.

The new methodology of treating a specular plate by using a virtual nozzle is crucial to solve the flowfield properties. In general, the approaches in the work can be extended to analyze collisionless free jet impingement, from exits with arbitrary shapes, onto plates of arbitrary shapes. It is also possible to adopt other specifically given VDFs (not necessary Maxwellian) for the nozzle exits and diffuse reflective surface.

This paper presented the ultimate solutions of collisionless free jet flows from a nozzle and jet impingement on a flat plate with diffuse and specular reflections. The work is more comprehensive and complex than the collisionless flowfield around a flat plate [26]. For polyatomic gas flows which involve translational and internal energy relaxations, or gas flows with multiple species, as long as they are collisionless, the methods in this paper are applicable as well.

Appendix: Several important integrals

$$\int_{-a}^{\infty}(k+a)e^{-k^2}dk=\frac{\sqrt{\pi}}{4}[1+\mathrm{erf}(a)](2a)+\frac{1}{2}e^{-a^2}$$

$$\int_{-a}^{\infty}(k+a)^2e^{-k^2}dk=\frac{\sqrt{\pi}}{4}[1+\mathrm{erf}(a)]\left(2a^2+1\right)+\frac{a}{2}e^{-a^2}$$

$$\int_{-a}^{\infty}(k+a)^3e^{-k^2}dk=\frac{\sqrt{\pi}}{4}[1+\mathrm{erf}(a)]\left(2a^3+3a\right)+\left(\frac{a^2}{2}+\frac{1}{2}\right)e^{-a^2}$$

$$\int_{-a}^{\infty}(k+a)^4e^{-k^2}dk=\frac{\sqrt{\pi}}{4}[1+\mathrm{erf}(a)]\left(2a^4+6a^2+\frac{3}{2}\right)+\left(\frac{a^3}{2}+\frac{5}{4}a\right)e^{-a^2}$$

$$\int_{-a}^{\infty}(k+a)^5e^{-k^2}dk=\frac{\sqrt{\pi}}{4}[1+\mathrm{erf}(a)]\left(2a^5+10a^3+\frac{15}{2}a\right)+\left(\frac{a^4}{2}+\frac{9}{4}a^2+1\right)e^{-a^2}$$

https://doi.org/10.4208/cicp.OA-2016-0165 Published online by Cambridge University Press

References

[1] R. Campargue, Historical account and branching to rarefied gas dynamics of atomic & molecular beams: A continuing and fascinating Odyssey commemorated by Nobel prizes awarded to 23 Laureates in physics & chemistry. 24th International Rarefied Gasdynamics Symposium, July, 2004.

[2] G. Sanna, and G. Tomassetti, *Introduction to Molecular Beams Gas Dynamics*, Imperial College Press, London, 2005.

[3] R. Maev, and V. Leshchynsky, *Introduction to Low Pressure Gas Dynamic Spray*, Wiley-Vch, Weinheim, Germany, 2008.

[4] D. Hastings, and H. Garrett, *Spacecraft-Environment Interactions*, Cambridge University Press, Cambridge, UK., 1996.

[5] P. Metzger, Rocket exhaust cratering: A serious challenge for space exploration. Proceedings of the 1st Workshop on Granular Materials in Lunar and Martian Exploration, KSC FL, Feb. 2-3, 2005.

[6] G.J. LeBeau, and F.E. Lumpkin, Application highlights of the DSMC Analysis Code (DAC) software for simulating rarefied flows, Comput. Method Appl. Math., 191(2011), pp.595-609. http://dx.doi.org/10.1016/S0045-7825(01)00304-8.

[7] K.C. Kannenberg, and I.D. Boyd, Three-dimensional Monte Carlo simulation of plume impingement, J. Thermophys. Heat Tr., 13(1999), No.2, pp.226-235. http://dx.doi.org/10.2514/2.6440.

[8] G.A. Simons, Effects of nozzle boundary layers on rocket exhaust plumes, AIAA J., 10(1972), No.11, pp.1534-1535. http://dx.doi.org/10.2514/3.6656.

[9] P. Vashchenov, A. Kudryavstev, D. Khotyanovsky, and M. Ivanov, DSMC and Navier-Stokes study of backflow for nozzle plumes expanding into vacuum. International Symposium on Rarefied Gas Dynamics (24th), Monopoli (Bari), Italy on 10-16, July 2004.

[10] W.G. Vincenti, and C.H. Kruger, *Introduction to Physical Gas Dynamics*, Krieger Publishing, Malabar, Florida, 1986.

[11] H.G. Noller, Approximate calculation of expansion of gas from nozzles into high vacuum, J. Vac. Sci. Tech., 3(1966), pp.202-207.

[12] R. Narasimha, Collisionless expansion of gases into vacuum, J. Fluid Mech., 12(1962), No.2., pp.294–308. https://doi.org/10.1017/S0022112062000208.

[13] M.S. Woronowicz, and N. Rault, On jet flowfield analysis and simulation techniques. AIAA paper 1994-2048, 6th AIAA/ASME Joint Thermophysics and Heat Transfer Conference, June 20-23, 1994, Colorado Springs, CO.

[14] C. Cai, and C. Zou, A gaskinetic study on planar collisionless jet impingement at a plate, Comm. Comput. Phys., 4(2013), pp.960-978.

[15] C. Cai, and X. Huang, High speed rarefied round jet impingement flows, AIAA J., 50(2012), pp.2908-2911. DOI: 10.2514/1.J051785.

[16] C. Cai, and X. He, Comprehensive investigations of high Knudsen number planar jet impingement on an inclined flat plate, Phys. Fluids, May, 2016.

[17] C. Cai, Gaskinetic modeling on dilute gaseous plume impingement flows, Aerospace, 3(2016), 43. DOI: 10.3390/aerospace3040043.

[18] C. Cai, and I.D. Boyd, Theoretical and numerical study of several free molecular flow problems, J. Spacecraft Rockets, 44(May-June, 2007), No.3, pp.619-624.

[19] C. Cai, and I.D. Boyd, Collisionless gas flow expanding into vacuum, J. Spacecraft Rockets, 44(2007), pp.1326-1330. DOI: 10.2514/1.32173.

https://doi.org/10.4208/cicp.OA-2016-0165 Published online by Cambridge University Press

[20] K. Khasawneh, H. Liu, and C. Cai, Surface properties for rarefied circular jet impingement on a flat plate, Phys. Fluids, 23(2011), pp.1-6. DOI: 10.1063/1.3549934.
[21] G.A. Bird, *Molecular Gas Dynamics and the Direct Simulation of Gas Flows.* Oxford University Press, New York, 1994.
[22] I.D. Boyd, Modelling of satellite control thruster plumes. Ph.D. Dissertation, Dept. of Aeronautics and Astronautics, University of Southampton, Southmpton, England, 1998.
[23] J.P.W. Stark, and I.D. Boyd, Modelling of a small hydrazine thruster plumes in the transition flow regime, J. Propul. Power, 6(1990), No.2, pp.121-126. http://dx.doi.org/10.2514/3.23232.
[24] E. Roohi, and S. Stefanov, Collision partner selection schemes in DSMC: From micro/nano flows to hypersonic flows, Phys. Reports, 656(2016), pp.1-38. http://dx.doi.org/10.1016/j.physrep.2016.08.002.
[25] H. Liu, and C. Cai, An object-oriented serial and parallel DSMC simulation package, Comput. & Fluids. 57(2012), pp.65-75.
[26] C. Cai, Analytical solutions for free-molecular gas flow over a flat plate, 29th International Rarefied Gasdynamics Symposium, Xi'an, China, July 12th-19th, 2014.

https://doi.org/10.4208/cicp.OA-2016-0165 Published online by Cambridge University Press